

# Low-frequency whistler waves excited by relativistic laser pulses

Huai-Hang Song,<sup>1,4</sup> Wei-Min Wang,<sup>2,1,5,\*</sup> Jia-Qi Wang,<sup>3</sup> Yu-Tong Li,<sup>1,4,5,6,†</sup> and Jie Zhang<sup>1,5,7</sup>

<sup>1</sup>*Beijing National Laboratory for Condensed Matter Physics,  
Institute of Physics, CAS, Beijing 100190, China*

<sup>2</sup>*Department of Physics and Beijing Key Laboratory of Opto-electronic Functional Materials and Micro-nano Devices,  
Renmin University of China, Beijing 100872, China*

<sup>3</sup>*College of Physical Science and Technology, Sichuan University, Chengdu 610065, China*

<sup>4</sup>*School of Physical Sciences, University of Chinese Academy of Sciences, Beijing 100049, China*

<sup>5</sup>*Collaborative Innovation Center of IFSA, Shanghai Jiao Tong University, Shanghai 200240, China*

<sup>6</sup>*Songshan Lake Materials Laboratory, Dongguan, Guangdong 523808, China*

<sup>7</sup>*Key Laboratory for Laser Plasmas, Ministry of Education,  
Shanghai Jiao Tong University, Shanghai 200240, China*

(Dated: October 16, 2020)

It is shown by multi-dimensional particle-in-cell simulations that intense secondary whistler waves with special vortex-like field topology can be excited by a relativistic laser pulse in the highly magnetized, near-critical density plasma. Such whistler waves with lower frequencies obliquely propagate on both sides of the laser propagation axis. The energy conversion rate from laser to whistler waves can exceed 15%. Their dispersion relations and field polarization properties can be well explained by the linear cold-plasma model. The present work presents a new excitation mechanism of whistler modes extending to the relativistic regime and could also be applied in magnetically assisted fast ignition.

## I. INTRODUCTION

Whistler waves [1] were first discovered in the ionosphere [2] with audio frequencies. Since then, as a branch of electromagnetic modes in the magnetized plasma, the whistler wave and its excitation have been extensively studied in space plasmas [3], laboratory plasmas [4, 5], and solid-state plasmas [6, 7]. Hot electrons with the sufficient temperature anisotropy are considered to be the dominant energetic source to stimulate whistler waves in the radiation belts [8, 9]. Modulated electron beams are the useful tools to trigger whistler waves via various wave-particle resonances [10, 11]. Magnetic antennas can generate whistler wave packets with helical phase fronts [12]. The Čerenkov whistler emission is also found in the magnetic reconnection [13, 14].

Recently, the whistler wave has also aroused interest in laser-plasma interactions, particularly in fast ignition, with the emergence of unprecedented strong magnetic fields up to the kilo-tesla level [15]. The strong magnetic fields lasting a few nanoseconds were experimentally produced at the center of coil targets driven by high-power nanosecond laser pulses [15–17]. With the assistance of such an external magnetic field, high-energy electron beams can be well guided in a high-density fusion fuel and the heating efficiency to the fuel can be significantly enhanced in the fast ignition, as shown in both simulations [18, 19] and experiments [20, 21]. Higher laser energies and optimized coil targets are expected to further increase the external magnetic field strength. When the external magnetic field exceeds a critical value

$B_c = m_e c \omega_0 / |e|$  (in Gaussian units), which means that the non-relativistic electron cyclotron frequency  $\omega_{ce}$  exceeds the laser frequency  $\omega_0$ , the laser-plasma interactions enter the whistler-mode regime, where  $m_e$  is the electron rest mass and  $e$  is the electron charge. In this case, the laser pulse can penetrate into an overdense plasma for a long distance due to the absence of cutoff density [22, 23]. Based on this unique property, a few theoretic works have shown the enhanced electron heating [24, 25], cyclotron resonance absorption [26], and wave to ion energy transfer [27, 28] in this regime. In these works, direct whistler-mode conversion was investigated in the highly magnetized overdense plasma that the laser pulse was considered as a whistler wave with the unchanged frequency before and after entering the plasma. In addition to this kind of direct whistler-mode conversion, intense laser interactions with the magnetized plasma may excite diverse and complicated secondary whistler waves of broad frequencies, for example, through whistler instabilities induced by electron flows [29, 30].

In this paper, we investigate low-frequency, secondary whistler wave excitation in the interaction of a relativistically intense laser pulse with a highly magnetized near-critical density plasma. For the laser penetration in overdense plasmas [24–28], this kind of secondary whistler wave emissions should also be taken into account since a lower-density preplasma usually is unavoidable. Our two-dimensional (2D) and three-dimensional (3D) particle-in-cell (PIC) simulations show that the excited whistler waves have special vortex-like field structures. The dispersion relation and field polarization properties of excited whistler waves are examined using a linear cold-plasma model.

In Sec. II, we present the PIC simulation results to show the field topology and time evolution of the excited

\* weiminwang1@ruc.edu.cn

† ytli@iphy.ac.cn

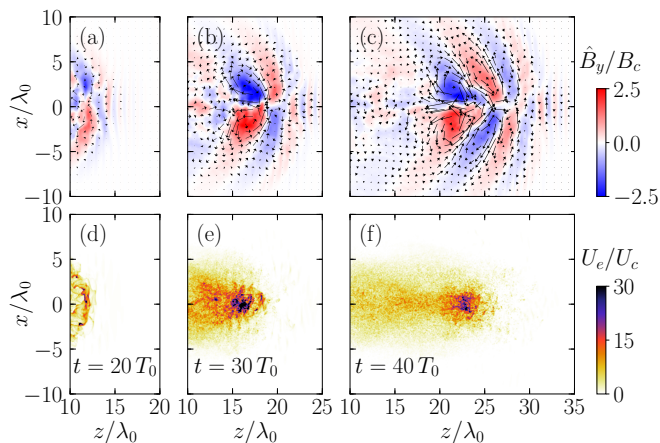


FIG. 1. Snapshots of azimuthal magnetic field  $\hat{B}_y$  (top row) and energy density of electrons  $U_e$  (bottom row) at three different times [(a), (d)]  $t = 20T_0$ , [(b), (e)]  $t = 30T_0$ , and [(c), (f)]  $t = 40T_0$ , where  $U_c$  is  $n_c m_e c^2$ . Vector plots of the magnetic field  $(\hat{B}_x, \hat{B}_z)$  in the  $x$ - $z$  plane are also presented in (a)-(c) to show the field topology.

whistler waves. In Sec. III, we give a qualitative picture about the whistler excitation mechanism. In addition, the dispersion relation as well as field polarization of whistler waves is analyzed based on a cold-plasma model. In Sec. IV, we discuss the impacts of parameters of the laser pulse, plasma density, and external magnetic field on the whistler wave excitation, and a 3D simulation is carried out. Section V contains a brief conclusion.

## II. SIMULATION RESULTS

To study the whistler wave excitation, we carry out a series of 2D and 3D relativistic PIC simulations. The main results are given by 2D PIC simulations due to a lower computational expense. Then, a 3D simulation is performed to further confirm the field topology of excited whistler waves.

In the first 2D simulation, a laser pulse with a profile of  $a_L = a_0 \sin^2(\pi t/\tau_0) \times \exp(-r^2/r_0^2)$  within  $0 < t \leq \tau_0$  is normally incident from the left boundary (at  $z = 0$ ). We take the laser normalized peak strength  $a_0 = |e|E_L/m_e c \omega_0 = 5.0$ , spot size  $r_0 = 4\lambda_0$ , and pulse duration  $\tau_0 = 20T_0$ , where  $T_0 = 2\pi/\omega_0$  is the laser period,  $\lambda_0 = 2\pi/k_0$  is the laser wavelength, and  $k_0$  is the laser wavenumber. At the initial moment  $t = 0$ , the plasma is composed of cold electrons and protons ( $m_p/m_e = 1836$ ). The computational domain has a size of  $60\lambda_0 \times 110\lambda_0$  in  $x \times z$  directions with  $1920 \times 3520$  cells. A vacuum is located at  $0 < z \leq 5\lambda_0$ , a low density plasma with an exponential ramp from  $0.01n_c$  to  $0.8n_c$  is within  $5 < z \leq 10\lambda_0$ , and a uniform plasma with a density of  $n_0 = 0.8n_c$  is followed at  $z > 10\lambda_0$ , where  $n_c = m_e \omega_0^2 / 4\pi e^2$  is the critical density. A uniform external magnetic field with a magnitude  $B_0 = 3.0B_c$  is imposed along the laser pulse

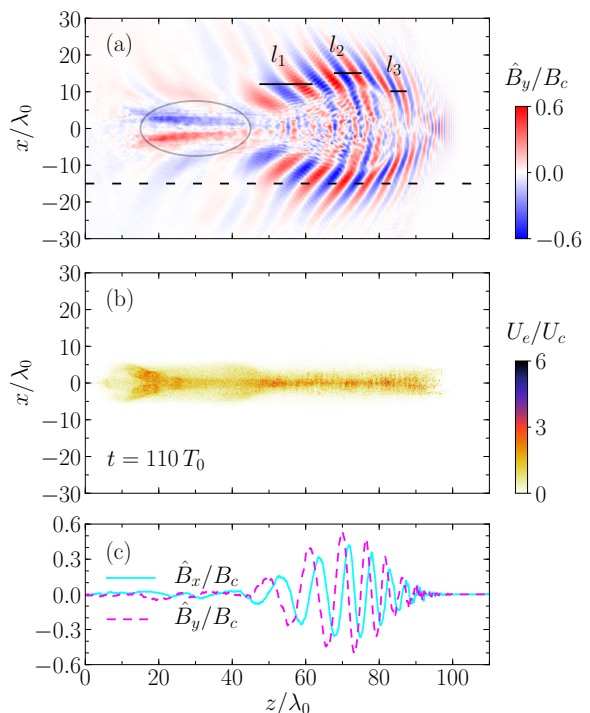


FIG. 2. Snapshots of (a) azimuthal magnetic field  $\hat{B}_y$  and (b) electron energy density  $U_e$  at  $t = 110T_0$ . We choose three local whistler segments along the  $z$  direction, as indicated by the solid lines  $l_1$ ,  $l_2$ , and  $l_3$  in (a), to further analyze the field polarization in detail in Fig. 6. (c) One-dimensional spatial profiles of  $\hat{B}_x$  and  $\hat{B}_y$  components taken from  $x = -15\lambda_0$  as indicated by the dashed line in (a).

propagation direction (i.e., along the  $+z$  axis). Each cell contains 16 macroparticles for each species. To reduce the numerical heating, the fourth-order interpolation [31] is applied. Absorbing boundary conditions are used for both particles and fields in any direction.

Figures 1(a)-1(c) show the spatial distributions of the out-of-plane or azimuthal magnetic field  $\hat{B}_y$  and in-plane magnetic field vector  $(\hat{B}_x, \hat{B}_z)$  at different times, displaying the formation of whistler waves as the laser pulse penetrates into the plasma. Here, we add a hat symbol  $\hat{\phantom{x}}$  over a variable to mean that the relevant quantity is averaged over one laser period in order to filter out the fast-varying laser field. Note that the axial magnetic component  $\hat{B}_z$  or  $B_z$  excludes the external magnetic field  $B_0$ . It can be seen that strong whistler waves are excited with a strength of  $2.5B_c$  in the  $\hat{B}_y$  component, which approaches the external magnetic field strength of  $3.0B_c$ . The whistler waves are right-hand circularly polarized through the field linkage between  $\hat{B}_y$  and  $(\hat{B}_x, \hat{B}_z)$  as shown in Figs. 1(b) and 1(c), similar to spheromak-like field perturbations observed in the laboratory plasma [32, 33]. In addition, the excited whistler waves have a cone-shaped phase structure due to their oblique propagation along the external magnetic field. The complete 3D field topology will be shown by a 3D PIC simula-

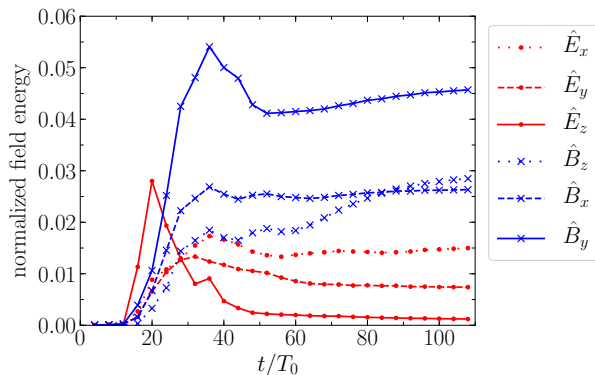


FIG. 3. Temporal evolution of energy of the electric and magnetic fields averaged by one laser period. Each energy component is normalized by the total laser energy.

tion later in Fig. 10. In Figs. 1(d)-1(f), we display the corresponding energy density distribution of electrons. Electrons in the laser interaction zone are rapidly accelerated up to tens of MeV. These high-energy electrons are strongly confined in the transverse direction by the external magnetic field.

The whistler waves gradually develop to have more wave cycles with time and higher-frequency components go ahead, as shown in Fig. 2(a) at a later time of  $t = 110T_0$ . This is because the higher-frequency whistler waves have higher group velocities in the plasma. Stable whistler waves obliquely propagate on both sides of the laser propagation axis, with wide local wave normal angles in the range of  $-50^\circ$  and  $50^\circ$ . The local wave normal angle is defined as the one between the local whistler wave vector  $\mathbf{k}$  and external magnetic field direction. We show a one-dimensional magnetic field distribution along  $x = -15\lambda_0$  in Fig. 2(c). The handedness of  $\pi/4$  phase shifting between  $\hat{B}_x$  and  $\hat{B}_y$  confirms its right-hand polarization with respect to the external magnetic field. Figure 2(b) is the corresponding electron energy density, showing that hot electrons are mainly confined around the laser propagation axis within a narrow zone by the strong external magnetic field. Obliquely propagating whistler waves spread in a broader zone where electrons have low energies and are still cold. One can analyze the whistler dynamics by a cold plasma model, as we will do in Sec. III. At the center area, the whistler field pattern looks turbulent and complex due to high-energy electron dynamics.

Figure 3 gives the energy evolution of one-laser-period-averaged (low-frequency) field components with time. The laser pulse impinges the plasma in the interval  $10T_0 < t < 30T_0$ , leading to a significant increase of whistler wave energy. Meanwhile, the whistler wave with its low frequency and high intensity can be depleted by the hot plasma since it is basically near the laser interaction zone in this time. As whistler wave generation and depletion are roughly counteracted, its field energy reaches the maximum at about  $t = 30T_0$ . Af-

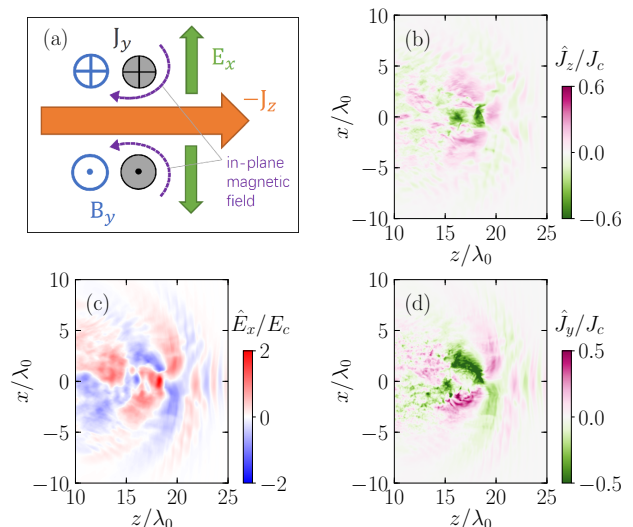


FIG. 4. (a) Schematic of whistler wave excitation. Snapshots of (b) axial current  $\hat{J}_z$ , (c) radial electric field  $\hat{E}_x$ , and (d) azimuthal current  $\hat{J}_y$  at  $t = 30T_0$  from the simulation, where  $E_c$  is  $m_e c \omega_0 / |e|$  and  $J_c$  is  $n_c |e| c$ . The azimuthal magnetic field component  $\hat{B}_y$  is induced by the strong axial current  $\hat{J}_z$ , and the in-plane magnetic field component ( $\hat{B}_x, \hat{B}_z$ ) is induced by the azimuthal Hall current  $\hat{J}_y$ .

ter  $t = 50T_0$ , the residual energy of each field component remains nearly constant with time, suggesting the stable, non-dissipative whistler wave propagation in the cold plasma region. The whistler wave carries about 9% of the total laser energy. The energy of magnetic fields ( $\sim 7\%$ ) is relatively higher than that of electric fields ( $\sim 2\%$ ), where the energy of axial electric component  $\hat{E}_z$  is almost zero due to a very high conductivity along the external magnetic field direction. The slight increases of  $\hat{B}_y$  and  $\hat{B}_z$  energies after  $t = 60T_0$  are attributed to quasi-static magnetic field growth in the left high-energy electron region as marked by an elliptic curve in Fig. 2(a), independent of propagating whistler waves.

### III. THEORETICAL ANALYSIS

The whistler wave excitation can be understood in electron magnetohydrodynamic regime by a simple 2D physical picture as sketched in Fig. 4(a). When a relativistically intense laser pulse propagates through a near-critical plasma, a ion channel can be formed [34, 35] by the laser pondermotive force. This pondermotive force pushes electrons both forward and laterally, resulting in a strong axial current  $\hat{J}_z$ , azimuthal magnetic field  $\hat{B}_y$ , and radial electric field  $\hat{E}_x$ , as shown in Figs. 4(b), 1(b), and 4(c), respectively. With an external magnetic field along the laser propagation direction, an azimuthal Hall current  $\hat{J}_y$  shown in Fig. 4(d) is also driven by the radial electric field  $\hat{E}_x$  through  $\mathbf{E} \times \mathbf{B}_0$  electron drifts, hence in-

ducing the in-plane magnetic field as shown in Fig. 1(b). The superposition of azimuthal and in-plane magnetic fields forms the observed vortex-like field structure. The similar whistler excitation by the electrode [36] or magnetic antenna [37] in non-relativistic regime has also been observed in discharge plasmas.

Then, a linear theory based on a cold magnetized plasma approximation is adopted here to study the properties of excited whistler waves, due to the fact that the whistler waves are obliquely propagating and mainly located outside the laser interaction zone where electrons have low energies. In the model, we ignore the motion of ions and collision effects, which is appropriate in the interaction between a relativistically ultrashort laser pulse and near-critical plasma. Because the whistler waves discussed here have broad spectra and their high-frequency components are close to the plasma frequency  $\omega_{pe} = \sqrt{4\pi n_e e^2/m_e}$ , the widely used dispersion formula of whistler modes  $c^2 k^2 = \omega \omega_{pe}^2 / (\omega_{ce} \cos \theta - \omega)$  cannot hold well, particularly in the present case of  $\omega_{pe} \lesssim \omega_{ce}$  [1]. Here,  $\theta$  is the local wave normal angle and  $\omega_{ce} = |e|B_0/m_e c$ . In our case with the external magnetic field along the  $+z$  axis and the whistler wave propagates in the  $x$ - $z$  plane, the general wave equation can be given by [38]

$$\begin{pmatrix} S - n^2 \cos^2 \theta & -iD & n^2 \cos \theta \sin \theta \\ iD & S - n^2 & 0 \\ n^2 \cos \theta \sin \theta & 0 & P - n^2 \sin^2 \theta \end{pmatrix} \begin{pmatrix} E_x \\ E_y \\ E_z \end{pmatrix} = 0 \quad (1)$$

where  $S = \frac{1}{2}(R + L)$ ,  $D = \frac{1}{2}(R - L)$ ,  $P = 1 - \omega_{pe}^2/\omega^2$ ,  $R = 1 - \omega_{pe}^2/(\omega^2 - \omega\omega_{ce})$ ,  $L = 1 - \omega_{pe}^2/(\omega^2 + \omega\omega_{ce})$ , and  $n = ck/\omega$  is the refractive index. Note that  $\omega_{ce}$  is a positive value in this paper.

A nontrivial solution of Eq. 1 requires that the determinant of  $3 \times 3$  matrix is zero, which yields the well-known dispersion relation [38]

$$n^2 = \frac{B \pm F}{2A}, \quad (2)$$

where  $A = S \sin^2 \theta + P \cos^2 \theta$ ,  $B = RL \sin^2 \theta + PS(1 + \cos^2 \theta)$ , and  $F^2 = (RL - PS)^2 \sin^4 \theta + 4P^2 D^2 \cos^2 \theta$ .

To gain insight into the dispersion properties of excited whistler modes in our PIC simulation, we perform 3D fast Fourier transformation of magnetic field  $B_y$  in the region of  $10\lambda_0 < z < 100\lambda_0$  over the time domain of  $70T_0 < t < 110T_0$  to obtain the power spectral density  $|\tilde{B}_y(\omega, \mathbf{k})|^2$  in the  $\omega - \mathbf{k}$  space. Here  $k_x$  and  $k_z$  are the wave vector components along  $x$  and  $z$  directions, respectively, and they satisfy  $k^2 = k_x^2 + k_z^2$  and  $\tan \theta = k_x/k_z$ . We select two  $\omega - k$  spectral slices of wave normal angles  $27^\circ$  and  $63^\circ$  from the  $\omega - \mathbf{k}$  space, as shown in Figs. 5(a) and 5(b). The whistler modes at these two angles agree well with the theoretical dispersion relation (dashed curves) governed by Eq. 2. The simulation further shows that this magnetized plasma system also supports left-hand electromagnetic modes with frequencies

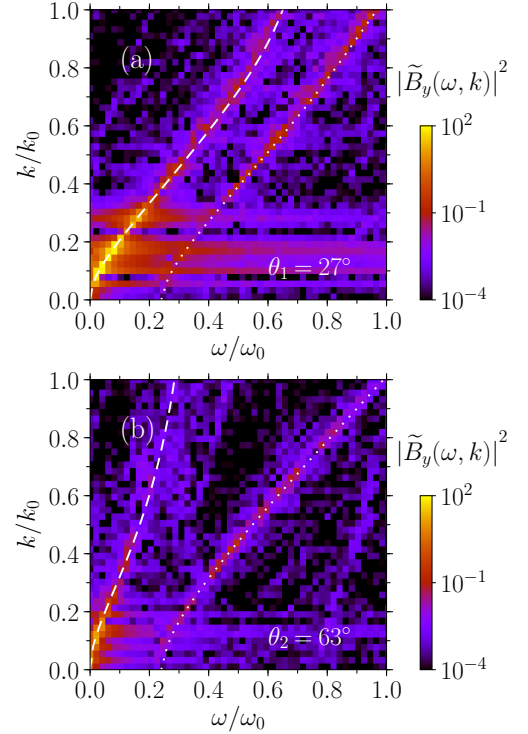


FIG. 5. The power spectral density of  $B_y$  at two selected wave normal angles (a)  $\theta_1 = 27^\circ$  and (b)  $\theta_2 = 63^\circ$  in the  $\omega - k$  coordinates, obtained from our PIC simulation. In each plot, the dashed curve stands for the theoretical whistler-mode dispersion relation given by Eq. 2 with  $\omega_{pe} = \sqrt{0.8}\omega_0$  and  $\omega_{ce} = 3.0\omega_0$  at the corresponding angles. The dotted curve stands for the theoretical dispersion relation of the left-hand wave.

higher than  $\frac{1}{2} \left( \sqrt{\omega_{ce}^2 + 4\omega_{pe}^2} - 3\omega_0 \right) = 0.246\omega_0$ . These much weaker left-hand modes also match the theoretical dispersion relation (dotted curves).

The wave polarization information in terms of electric field  $\mathbf{E}$  can be given by Eq. 1. Through simple operations, the ratios of electric field components can be characterized by

$$\frac{E_y}{E_x} = i \frac{D}{n^2 - S}, \quad \frac{E_z}{E_x} = \frac{n^2 \sin \theta \cos \theta}{n^2 \sin^2 \theta - P}. \quad (3)$$

With Faraday's law  $\nabla \cdot \mathbf{E} = -\frac{1}{c} \partial \mathbf{B} / \partial t$ , the ratios of the magnetic field components can be derived as

$$\frac{B_z}{B_x} = -\tan \theta, \quad \frac{B_y}{B_x} = \tan \theta \frac{E_z}{E_y} - \frac{E_x}{E_y}. \quad (4)$$

The ratio of  $B_z$  to  $B_x$  is completely determined by Maxwell's equations, thus it is a universal relation independent of the plasma behavior. Equation 3 and 4 can be further simplified with  $-P \gg 1$  and one can obtain  $E_z/E_x \approx 0$  and  $B_y/B_x \approx -E_x/E_y$ . It implies that longitudinal electric field  $E_z$  is negligible, which is consistent with the result in Fig. 3. With these simplifications and defining the dimensionless parameter  $\eta = |D/(n^2 - S)|$ ,

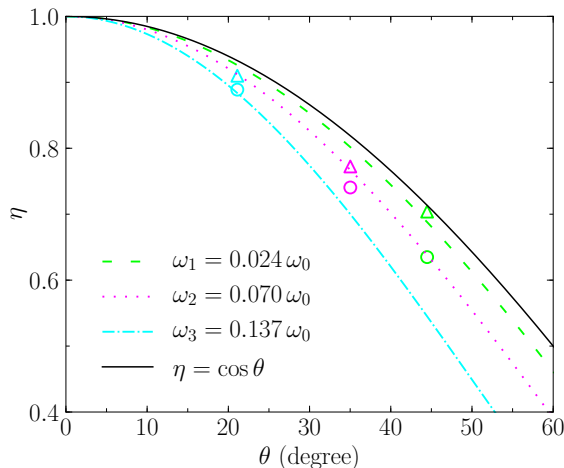


FIG. 6. The theoretical  $\eta$  as a function of  $\theta$  according to Eq. 1 at three different wave frequencies  $\omega_1 = 0.026\omega_0$  (dashed green curve),  $\omega_2 = 0.072\omega_0$  (dotted violet curve),  $\omega_3 = 0.156\omega_0$  (dot-dashed cyan curve), where  $\omega_{pe} = \sqrt{0.8}\omega_0$ ,  $\omega_{ce} = 3.0\omega_0$ .  $\omega_1$ ,  $\omega_2$  and  $\omega_3$  correspond to frequencies of three whistler segments  $l_1$ ,  $l_2$  and  $l_3$  indicated in Fig. 2(a), respectively. The limit solution  $\eta = \cos \theta$  is also plotted as a reference (black solid curve). Triangle and circle marks represent  $|B_x|/|B_y|$  and  $|E_y|/|E_x|$  values of these three whistler segments from the simulation with  $l_1$  in green,  $l_2$  in violet, and  $l_3$  in cyan.

the amplitude ratios of field components can be approximated as follows:

$$\frac{|B_x|}{|B_y|} \approx \frac{|E_y|}{|E_x|} = \eta, \quad \frac{|E_z|}{|E_x|} \approx 0, \quad \frac{|B_z|}{|B_x|} = |\tan \theta|. \quad (5)$$

The limits of small wave frequencies  $\omega \ll \omega_{pe}$  and  $\omega_{ce} < \omega_{pe}$  are well satisfied in typical magnetospheric plasmas and the relation  $\eta \approx |\cos \theta|$  is obtained [39, 40]. In this situation, the magnetic field is still circularly polarized even for obliquely propagating whistler waves, while the electric field is circularly polarized only in the direction transverse to the wave vector. In our case with  $\omega_{ce} > \omega_{pe}$ , the relation  $\eta \approx |\cos \theta|$  still holds but with a higher requirement for the limit of  $\omega \ll \omega_{pe}$ , as shown in Fig. 6.

To examine the whistler wave polarization, we select three single-cycle whistler segments at different positions as indicated by lines  $l_1$ ,  $l_2$ , and  $l_3$  in Fig. 2(a). Each line is parallel to the  $x$  axis. For each whistler segment, we treat it as a plane wave, so Eq. 5 can be applied. The local wave normal angle can be inferred through the ratio of  $|B_z|$  to  $|B_x|$  in Eq. 5 due to its independence on specific electromagnetic modes. In practice, we use the sum of absolute values of each field segment to calculate their ratios. We estimate the wavenumber component  $k_z$  directly from Fig. 2(a) and then the wavenumber  $k = k_z/\cos \theta$  can be obtained. The refractive index  $n$  and frequency  $\omega$  can be calculated from the dispersion relation Eq. 2, since it has been confirmed by Fig. 5. The theoretic curves of  $\eta$  corresponding to each whistler seg-

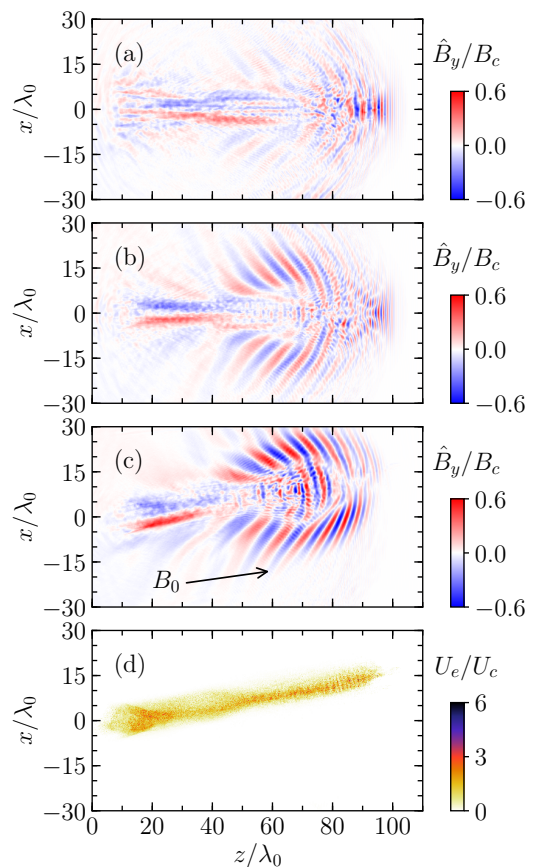


FIG. 7. Snapshots of azimuthal magnetic field  $\hat{B}_y$  at  $t = 110T_0$ , where the laser and external magnetic field parameters are identical to those of Fig. 2, but for (a) a left-hand circularly polarized laser, (b) a linear polarized laser, and (c) the obliquely imposed external magnetic field with an angle of  $10^\circ$  to the  $+z$  axis. (d) Energy density of electrons  $U_e$  corresponding to (c).

ment are shown in Fig. 6. The field component ratios  $|B_x|/|B_y|$  and  $|E_y|/|E_x|$  obtained from the PIC simulation are marked by triangles and circles, respectively, in a good agreement with the theoretic curves. The ratio of  $|E_y|/|E_x|$  from each field segment is lower than the theoretic value, mainly because the  $|E_x|$  component is affected by electrostatic field under above estimates.

#### IV. IMPACTS OF LASER, PLASMA, AND MAGNETIC-FIELD PARAMETERS

We proceed to investigate the impact of laser parameters on the whistler wave excitation. First, the laser pulse should be relativistically intense ( $a_0 > 1$ ). Below the relativistic strength, the laser field behavior follows the linear dispersion relation given by Eq. 2, suggesting that secondary emissions with frequencies different from the laser frequency cannot be triggered.

The laser polarization also plays a crucial role. Above,

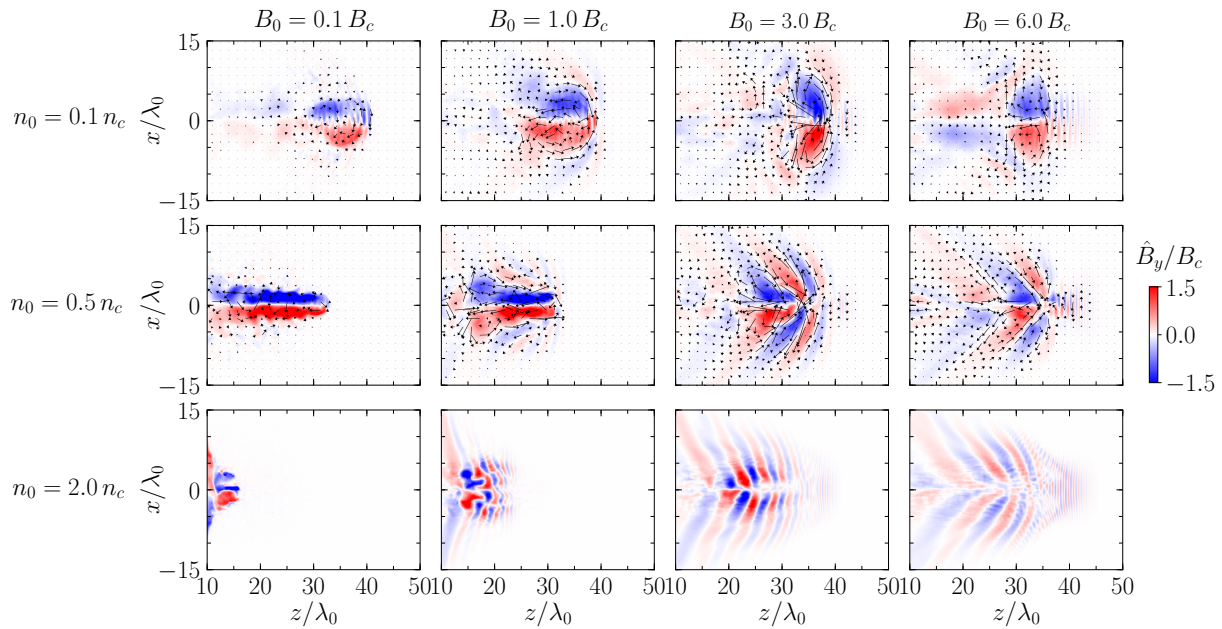


FIG. 8. Snapshots of azimuthal magnetic field  $\hat{B}_y$  at  $t = 50T_0$  under different external magnetic field strengths  $B_0 = 0.1B_c$  (first column),  $1.0B_c$  (second column),  $3.0B_c$  (third column), and  $6.0B_c$  (fourth column), as well as different plasma densities  $n_0 = 0.1n_c$  (first row),  $0.5n_c$  (second row), and  $2.0n_c$  (third row). Vector plots of the magnetic field ( $\hat{B}_x$ ,  $\hat{B}_z$ ) in the  $x$ - $z$  plane are also presented in the first two rows.

we have taken the right-hand circularly polarized laser pulse, and consequently strong right-hand circularly polarized whistler waves are observed. When we change the laser polarization to be left-hand in Fig. 7(a), the low-frequency field looks much weaker compared with that of Fig. 2(a). The high dependence on laser polarization may seem strange because whistler waves are driven by the electron currents due to laser pondermotive force as described in Fig. 4. One possible reason is that the right-hand circularly polarized laser pulse interacts more strongly with the magnetized plasma than the left-hand laser, hence it can drive more strong electron currents to excite whistler waves. The complex interaction among laser field, plasma, and whistler wave in the relativistic region is still to be studied. We further set the laser pulse to be linearly polarized along the  $x$  axis with an amplitude of  $a_0 = 5\sqrt{2}$  to keep the total laser intensity unchanged. In Fig. 7(b), the excited whistler waves are stronger than those by the left-hand polarized laser pulse in Fig. 7(a), but weaker than those by the right-hand one in Fig. 2(a), since a linear polarization can be decomposed into a left-hand polarization and a right-hand one.

In Figs. 7(c) and 7(d), we take the external magnetic field has a angle  $10^\circ$  with respect to the laser propagation direction (the  $+z$  axis). The excited whistler waves have a similar pattern to the co-directed configuration shown in Fig. 2(a), but the pattern axis is along the direction of the external magnetic field, rather than the laser propagation direction. This can be explained by the generated hot electrons strongly confined along the external mag-

netic field direction, as shown in Fig. 7(d). Therefore, the central axis of the whistler wave pattern is mainly determined by the external magnetic field.

In Fig. 8, we scan the plasma density  $n_0$  and external magnetic field strength  $B_0$ , while keeping other param-

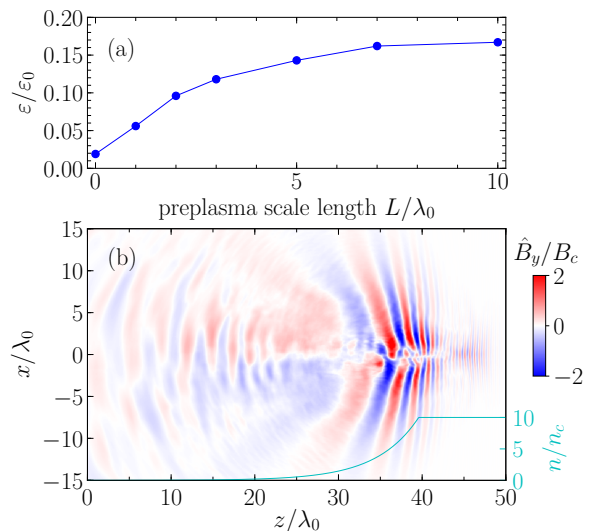


FIG. 9. (a) The low-frequency whistler conversion rate  $\varepsilon/\varepsilon_0$  versus preplasma scale lengths  $L$ , where  $\varepsilon$  and  $\varepsilon_0$  are the whistler wave energy and the total laser energy, respectively. (b) Snapshot of azimuthal magnetic field  $\hat{B}_y$  at  $t = 50T_0$  in the case of  $L = 5\lambda_0$ . The spatial profile of initial plasma density  $n$  is also given.

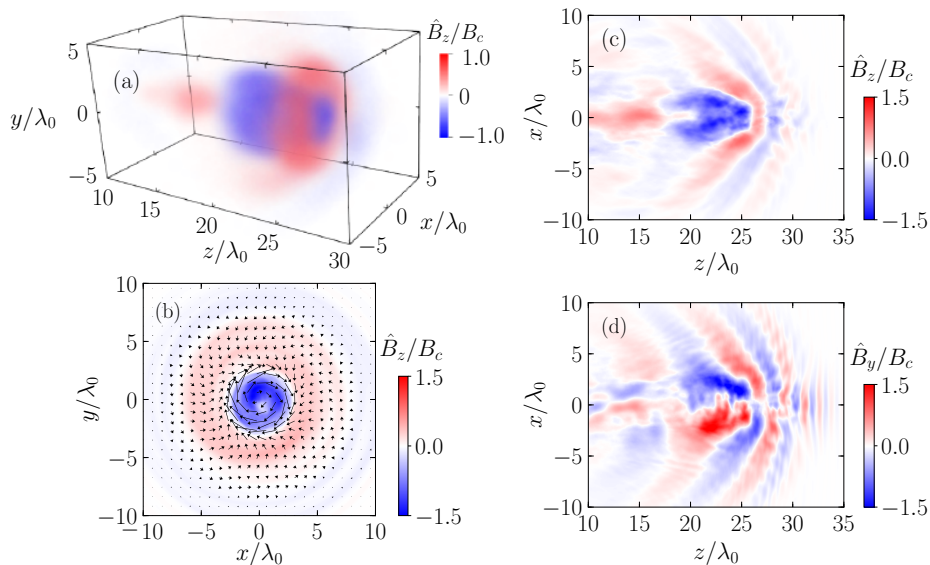


FIG. 10. 3D simulation results at  $t = 30 T_0$ . (a) Profile of axial magnetic field  $\hat{B}_z$  in the 3D volume view. (b) Snapshot of axial magnetic field  $\hat{B}_z$  associated with the vector plot of  $(\hat{B}_x, \hat{B}_y)$  at  $z = 22\lambda_0$  in the  $x$ - $y$  plane. [(c), (d)] Snapshots of  $\hat{B}_z$  and  $\hat{B}_y$  at  $y = 0$  in the  $x$ - $z$  plane.

eters the same as those in Fig. 2. For a plasma density much lower than the critical one (see  $n_0 = 0.1n_c$  cases in Fig. 8), a stable spheromak-like whistler wave packet can be formed, which is different from the typical multi-cycle whistler waves in a higher density plasma at the same time (see  $n_0 = 0.5n_c$  or  $n_0 = 2.0n_c$  cases in Fig. 8), but similar to their early states (see the  $n_0 = 0.8n_c$  case in Fig. 2(b)). Besides, the excited whistler waves are weaker as the plasma density increases to over  $n_c$  (see  $n_0 = 2.0n_c$  cases in Fig. 8). This illustrates advantages of near-critical density for whistler wave excitation and agrees with the below results in Fig. 9 that the whistler wave conversion is much lower in the absence of low-density preplasma. By comparing these cases under different external magnetic field strengths, we can find that strong whistler waves can be excited only when  $B_0$  exceeds  $B_c$ . Below the critical strength  $B_c$ , the generated azimuthal magnetic fields are primarily quasi-static fields, not waves. Note that the condition  $B_0 > B_c$  is also required for the laser penetration in overdense plasma [24–28]. From this point of view, this kind of secondary whistler wave emission should also be taken into account even in the study of overdense plasmas if a relativistic intense laser is employed, since a low-density preplasma at the front surface usually is unavoidable, particularly in fast ignition [41].

To illustrate the influence of preplasma on the low-frequency whistler wave conversion in the interaction of laser pulse with strongly magnetized overdense plasmas, we take an overdense plasma with a density of  $10n_c$  and in the front of it there is a preplasma with an exponential density profile of a scale length  $L$ . Other simulation parameters are the same as Fig. 2. The energy of excited low-frequency whistler waves normalized

by the total laser energy is shown in Fig. 9(a). For a steep overdense interface of  $L = 0$ , the conversion ratio is less than 0.02. Taking into account relativistic effects, the corrected critical density in this case is increased to  $n_c^* = n_c \sqrt{1 + a_0^2} \approx 5n_c$ , hence there is still a small whistler conversion ratio when  $L = 0$  and  $n_0 = 10n_c \approx 2n_c^*$ . The conversion ratio is expected to be much less than 0.02 for a higher-density plasma without the preplasma. With increasing the preplasma scale length, the conversion ratio rises up dramatically, and it saturates up to 0.16 at  $L = 10\lambda_0$ . Thus, the excitation process of low-frequency whistler waves in the preplasma region should be taken into account, at least in terms of energy share. Figure 9(a) shows the azimuthal magnetic field component  $\hat{B}_y$  in a representative case of  $L = 5\lambda_0$ , we can see strong whistler waves are excited in the preplasma and then they propagate deep into the overdense plasma region due to the absence of cutoff density.

Finally, we conduct a 3D PIC simulation, to demonstrate the 3D field topology of whistler waves. We take a simulation box of  $30\lambda_0 \times 30\lambda_0 \times 30\lambda_0$  in  $x \times y \times z$  directions with  $480 \times 480 \times 480$  cells. Each cell contains 8 macroparticles for each species. Other parameters are still the same as those in Fig. 2. The field distribution of axial magnetic component  $\hat{B}_z$  at  $t = 30T_0$  via a 3D volume view is shown in Fig. 10(a). Its two central slices in the  $x$ - $y$  plane and  $x$ - $z$  plane are also shown in Fig. 10(b) and 10(c), respectively. It can be seen that the axial component  $\hat{B}_z$  is almost axisymmetric with respect to the  $z$  axis. In Fig. 10(b), we also plot the azimuthal field vector  $(\hat{B}_x, \hat{B}_y)$ . The azimuthal magnetic field has a right-hand linkage with respect to the axial magnetic field. A central slice of  $\hat{B}_y$  in Fig. 10(d) is almost identi-

cal to that in Fig. 1(c) that we have obtained in the 2D PIC simulation.

To excite strong low-frequency whistler waves, the required external magnetic field strength should be higher than the critical magnetic field  $B_c$  from our simulations, which is determined by the laser wavelength  $\lambda_0$ . For Ti:Sapphire lasers with a typical wavelength  $\lambda_0 = 800$  nm,  $B_c \approx 13$  kT, which is about one order of magnitude higher than that achieved in present experiments [15–17]. For CO<sub>2</sub> lasers [42] with a wavelength of 10  $\mu$ m, the critical magnetic field can be significantly reduced to a more realistic value of  $B_c \approx 1$  kT.

## V. CONCLUSION

In summary, a series of 2D and 3D PIC simulations show that a relativistic laser pulse can excite low-frequency, vortex-like whistler waves in a highly magnetized, near-critical density plasma. The excited whistler modes at different wave normal angles obtained from PIC simulations are in agreement with the dispersion relation given by a cold-plasma theory. The theory also confirmed the field polarization properties. By scanning parameters

of plasma density and external magnetic field strength, we find that the whistler waves can be widely excited if  $B_0 > B_c$ , which is the same as the requirement for the direct whistler-mode conversion of laser pulses in overdense plasmas. This work enriches the whistler wave excitation mechanism and extends it to the relativistic interaction regime. These results could be referred in the magnetically assisted fast ignition study and a double-cone ignition (DCI) project recently funded in China [43].

## ACKNOWLEDGMENTS

This work was supported by the Strategic Priority Research Program of Chinese Academy of Sciences (Grant Nos. XDA25050300, XDA25010300, and XDB16010200), the National Key R&D Program of China (Grant No. 2018YFA0404801), National Natural Science Foundation of China (Grant Nos. 11775302, 11827807 and 11520101003), Science Challenge Project of China (Grant No. TZ2016005), the Fundamental Research Funds for the Central Universities, the Research Funds of Renmin University of China (20XNLG01), Sichuan Science and Technology Program No.2017JY0224, and the Innovation Spark Project of Sichuan University No. 2018SCUH0090.

- 
- [1] R. A. Helliwell, *Whistlers and Related Ionospheric Phenomena* (Stanford University Press Stanford, Calif., 1965).
  - [2] H. Barkhausen, “Zwei mit hilfe der neuen verstärker entdeckte erscheinungen,” *Phys. Z.* **20**, 401 (1919).
  - [3] B. T. Tsurutani and E. J. Smith, “Postmidnight chorus: A substorm phenomenon,” *J. Geophys. Res.* **79**, 118–127 (1974).
  - [4] R. L. Stenzel, “Whistler waves in space and laboratory plasmas,” *J. Geophys. Res.* **104**, 14379–14395 (1999).
  - [5] B. Van Compernelle, X. An, J. Bortnik, R. M. Thorne, P. Pribyl, and W. Gekelman, “Laboratory simulation of magnetospheric chorus wave generation,” *Plasma Phys. Control. Fusion* **59**, 014016 (2016).
  - [6] C. R. Leg ndy, “Macroscopic theory of helicons,” *Phys. Rev.* **135**, A1713–A1724 (1964).
  - [7] B. W. Maxfield, “Helicon waves in solids,” *Am. J. Phys.* **37**, 241–269 (1969).
  - [8] X. Fu, M. M. Cowee, R. H. Friedel, H. O. Funsten, S. P. Gary, G. B. Hospodarsky, C. Kletzing, W. Kurth, Brian A. Larsen, K. Liu, E. A. MacDonald, K. Min, G. D. Reeves, R. M. Skoug, and D. Winske, “Whistler anisotropy instabilities as the source of banded chorus: Van allen probes observations and particle-in-cell simulations,” *J. Geophys. Res.* **119**, 8288–8298 (2014).
  - [9] Y. Omura and D. Nunn, “Triggering process of whistler mode chorus emissions in the magnetosphere,” *J. Geophys. Res.* **116**, A05205, (2011).
  - [10] C. Krafft, P. Th venet, G. Matthieussent, B. Lundin, G. Belmont, B. Lemb ge, J. Solomon, J. Lavergnat, and T. Lehner, “Whistler wave emission by a modulated electron beam,” *Phys. Rev. Lett.* **72**, 649–652 (1994).
  - [11] X. An, J. Bortnik, and B. Van Compernelle, “Linear unstable whistler eigenmodes excited by a finite electron beam,” *Phys. Plasmas* **26**, 082114 (2019).
  - [12] R. L. Stenzel, “Whistler modes excited by magnetic antennas: A review,” *Phys. Plasmas* **26**, 080501 (2019).
  - [13] M. V. Goldman, D. L. Newman, G. Lapenta, L. Andersson, J. T. Gosling, S. Eriksson, S. Markidis, J. P. Eastwood, and R. Ergun, “Cherenkov emission of quasiparallel whistlers by fast electron phase-space holes during magnetic reconnection,” *Phys. Rev. Lett.* **112**, 145002 (2014).
  - [14] K. Steinvall, Y. V. Khotyaintsev, D. B. Graham, A. Vaivads, O. Le Contel, and C. T. Russell, “Observations of electromagnetic electron holes and evidence of cherenkov whistler emission,” *Phys. Rev. Lett.* **123**, 255101 (2019).
  - [15] S. Fujioka, Z. Zhang, K. Ishihara, K. Shigemori, Y. Hironaka, T. Johzaki, A. Sunahara, N. Yamamoto, H. Nakashima, T. Watanabe, *et al.*, “Kilotesla magnetic field due to a capacitor-coil target driven by high power laser,” *Sci. Rep.* **3**, 1170 (2013).
  - [16] J. J. Santos, M. Bailly-Grandvaux, M. Ehret, A. V. Arefiev, D. Batani, F. N. Beg, A. Calisti, S. Ferri, R. Florido, P. Forestier-Colleoni, *et al.*, “Laser-driven strong magnetostatic fields with applications to charged beam transport and magnetized high energy-density physics,” *Phys. Plasmas* **25**, 056705 (2018).
  - [17] Z. Zhang, B. J. Zhu, Y. T. Li, W. M. Jiang, D. W. Yuan, H. G. Wei, G. Y. Liang, F. L. Wang, G. Zhao, J. Y. Zhong, and *et al.*, “Generation of strong magnetic fields with a laser-driven coil,” *High Power Laser Sci. Eng.* **6**, e38 (2018).

- [18] D. J. Strozzi, M. Tabak, D. J. Larson, L. Divol, A. J. Kemp, C. Bellei, M. M. Marinak, and M. H. Key, “Fast-ignition transport studies: Realistic electron source, integrated particle-in-cell and hydrodynamic modeling, imposed magnetic fields,” *Phys. Plasmas* **19**, 072711 (2012).
- [19] W.-M. Wang, P. Gibbon, Z.-M. Sheng, and Y.-T. Li, “Magnetically assisted fast ignition,” *Phys. Rev. Lett.* **114**, 015001 (2015).
- [20] M. Bailly-Grandvaux, J. J. Santos, C. Bellei, P. Forestier-Colleoni, S. Fujioka, L. Giuffrida, J. J. Honrubia, D. Batani, R. Bouillaud, M. Chevrot, *et al.*, “Guiding of relativistic electron beams in dense matter by laser-driven magnetostatic fields,” *Nat. Commun.* **9**, 102 (2018).
- [21] S. Sakata, S. Lee, H. Morita, T. Johzaki, H. Sawada, Y. Iwasa, K. Matsuo, K. F. F. Law, A. Yao, M. Hata, *et al.*, “Magnetized fast isochoric laser heating for efficient creation of ultra-high-energy-density states,” *Nat. Commun.* **9**, 3937 (2018).
- [22] X. H. Yang, W. Yu, H. Xu, M. Y. Yu, Z. Y. Ge, B. B. Xu, H. B. Zhuo, Y. Y. Ma, F. Q. Shao, and M. Borghesi, “Propagation of intense laser pulses in strongly magnetized plasmas,” *Appl. Phys. Lett.* **106**, 224103 (2015).
- [23] S. X. Luan, W. Yu, F. Y. Li, Dong Wu, Z. M. Sheng, M. Y. Yu, and J. Zhang, “Laser propagation in dense magnetized plasma,” *Phys. Rev. E* **94**, 053207 (2016).
- [24] D. Wu, S. X. Luan, J. W. Wang, W. Yu, J. X. Gong, L. H. Cao, C. Y. Zheng, and X. T. He, “The controllable electron-heating by external magnetic fields at relativistic laser-solid interactions in the presence of large scale pre-plasmas,” *Plasma Phys. Control. Fusion* **59**, 065004 (2017).
- [25] J. X. Gong, L. H. Cao, K. Q. Pan, C. Z. Xiao, D. Wu, and X. T. He, “Enhancing the electron acceleration by a circularly polarized laser interaction with a cone-target with an external longitudinal magnetic field,” *Phys. Plasmas* **24**, 033103 (2017).
- [26] T. Sano, Y. Tanaka, N. Iwata, M. Hata, K. Mima, M. Murakami, and Y. Sentoku, “Broadening of cyclotron resonance conditions in the relativistic interaction of an intense laser with overdense plasmas,” *Phys. Rev. E* **96**, 043209 (2017).
- [27] T. Sano, M. Hata, D. Kawahito, K. Mima, and Y. Sentoku, “Ultrafast wave-particle energy transfer in the collapse of standing whistler waves,” *Phys. Rev. E* **100**, 053205 (2019).
- [28] T. Sano, S. Fujioka, Y. Mori, K. Mima, and Y. Sentoku, “Thermonuclear fusion triggered by collapsing standing whistler waves in magnetized overdense plasmas,” *Phys. Rev. E* **101**, 013206 (2020).
- [29] S. P. Gary, *Theory of space plasma microinstabilities* (Cambridge university press, 2005).
- [30] T. Taguchi, T. M. Antonsen, and K. Mima, “Stagnation of electron flow by a nonlinearly generated whistler wave,” *J. Plasma Phys.* **83**, 905830204 (2017).
- [31] T. Zh. Esirkepov, “Exact charge conservation scheme for particle-in-cell simulation with an arbitrary form-factor,” *Comput. Phys. Comm.* **135**, 144 – 153 (2001).
- [32] R. L. Stenzel, J. M. Urrutia, and K. D. Strohmaier, “Whistler modes with wave magnetic fields exceeding the ambient field,” *Phys. Rev. Lett.* **96**, 095004 (2006).
- [33] B. Eliasson and P. K. Shukla, “Dynamics of whistler spheromaks in magnetized plasmas,” *Phys. Rev. Lett.* **99**, 205005 (2007).
- [34] A. Pukhov and J. Meyer-ter-Vehn, “Relativistic magnetic self-channeling of light in near-critical plasma: Three-dimensional particle-in-cell simulation,” *Phys. Rev. Lett.* **76**, 3975–3978 (1996).
- [35] A. Pukhov, Z.-M. Sheng, and J. Meyer-ter-Vehn, “Particle acceleration in relativistic laser channels,” *Phys. Plasmas* **6**, 2847–2854 (1999).
- [36] J. M. Urrutia, R. L. Stenzel, and C. L. Rousculp, “Pulsed currents carried by whistlers. ii. excitation by biased electrodes,” *Phys. Plasmas* **1**, 1432–1438 (1994).
- [37] R. L. Stenzel, J. M. Urrutia, and C. L. Rousculp, “Pulsed currents carried by whistlers. part i: Excitation by magnetic antennas,” *Phys. Fluids* **5**, 325–338 (1993).
- [38] T. H. Stix, *Waves in plasmas* (American Institute of Physics, 1992).
- [39] O. P. Verkhoglyadova, B. T. Tsurutani, and G. S. Lakhina, “Properties of obliquely propagating chorus,” *J. Geophys. Res.* **115**, A00F19 (2010).
- [40] P. M. Bellan, “Circular polarization of obliquely propagating whistler wave magnetic field,” *Phys. Plasmas* **20**, 082113 (2013).
- [41] G. Li, R. Yan, C. Ren, T.-L. Wang, J. Tonge, and W. B. Mori, “Laser channeling in millimeter-scale underdense plasmas of fast-ignition targets,” *Phys. Rev. Lett.* **100**, 125002 (2008).
- [42] D. Haberberger, S. Tochitsky, and C. Joshi, “Fifteen terawatt picosecond co2 laser system,” *Opt. Express* **18**, 17865–17875 (2010).
- [43] J. Zhang, W. M. Wang, X. H. Yang, D. Wu, Y. Y. Ma, J. L. Jiao, Z. Zhang, F. Y. Wu, X. H. Yuan, Y. T. Li, and J. Q. Zhu, “Double-cone ignition scheme for inertial confinement fusion,” *Phil. Trans. R. Soc. A* **378**, 20200015 (2020).